The Effects of Variability in Plasmonic Nanoparticle Packing on Optical Scattering and Extinction Cross-section

Anil Yuksel
IBM Corporation
11400 Burnet Road
Austin, TX 78758, USA

Edward T. Yu
Department of Electrical and Computer Engineering
The University of Texas at Austin
Austin, TX 78758, USA

Michael Cullinan
Department of Mechanical Engineering
The University of Texas at Austin
Austin, TX 78712, USA

Jayathi Murthy
Henry Samueli School of Engineering and Applied Science
University of California, Los Angeles
Los Angeles, CA 90095, USA

ABSTRACT

Making photonic sintering of metal nanoparticles a viable nanomanufacturing process for printed electronics requires an understanding of all of the parameters that lead to variability in the photonic sintering process. This paper examines the effects of variability in the exact location of nanoparticles within a packing on the thermo-optical properties of the assemblies. Multiple Discrete Element Method (DEM) simulations for various nanoparticle packing configurations are created, and the absorption, scattering and extinction cross-sections for each of these configurations are calculated. The results of these simulations are then validated using experimental measurements on actual nanoparticle packings, and analyzed to determine how uncertainty in the initial nanoparticle packing configuration translates into variances in its calculated thermo-optical properties. Overall, it was found that simulations matched very well with the absorptivity measurements between 400 nm and 800 nm wavelength light illumination that uncertainty in the initial nanoparticle configuration resulted in about a 15-25 % variance in the thermo-optical properties of the nanoparticle packings for the analyzed cases.

KEY WORDS: Optical Plasmonics, Nanoparticle Packings, Thermo-Optical Properties

INTRODUCTION

Over the past decade, the ability to cheaply build custom electronics on a variety of substrates has allowed the field of printed electronics to make rapid advances [1, 2, 3]. This flexibility and versatility in the printed-electronics manufacturing process has proven to be important for a number of aerospace, biomedical and sensing applications [4, 5, 6]. In printed electronics manufacturing, nanoparticle inks are deposited onto a substrate using a variety of methods such as spin coating [7], ink jet printing [8], or aerosol jetting [9] and then photonically cured to create electrically conductive structures [10]. In the photonic sintering process the metal nanoparticles in the inks are exposed to high power laser energy, which causes the nanoparticles to heat up and sinter together [11, 12, 13]. From our previous work [14, 15, 16], it was observed that nanoparticle size, spacing and the distance between adjacent particles all potentially affect the thermo-optical properties and the plasmonic behavior of nanoparticles that are of interest to the photonic sintering. Therefore, selecting the correct processing parameters to optimize the photonic sintering is difficult since the exact configuration of the nanoparticles has a large effect on the localized surface plasmons that can be excited within the nanoparticle packing. These localized surface plasmons are important within the nanoparticle packings for the photonic sintering process because they can generate very intense, non-local electromagnetic energy, which drives the thermal energy transport within the packings [13, 17]. Furthermore, factors such as plasmonic mode structure and resonant frequency are highly dependent on the details of the interactions between metal nanoparticles and an underlying dielectric substrate. Different packing arrangements could, therefore, yield substantially different thermal transport and sintering behavior. Thus, it is important to understand how the exact configuration of nanoparticles within the nanoparticle packing affects the thermo-optical properties of the packing, in order to design photonic sintering processes that are robust to variances in nanoparticle configuration and that will produce the best post-cured metal structures.

To this end, multiple nanoparticle packings were generated for this study and an uncertainty analysis was performed to assess the effects of variability in the nanoparticle packing configuration on the thermo-optical properties of the

nanoparticle packings. In particular, four different nanoparticle packings were generated using identical particle size distributions and that are 1 μm x 1 μm in area and ~400 nm in thickness. Both the particle size distributions and packing thicknesses were chosen to match those used in a typical microscale selective laser sintering system [10]. These results were used to investigate the sensitivity of the thermo-optical properties to detailed particle packing configuration for these four randomly generated packings, and the corresponding effects on near-field interactions. Ultimately, these results will be used to predict the nanoparticle packing's temperature on the substrate and to provide insights into interconnect part formation in processes that utilize photonic sintering.

COMPUTATIONAL APPROACH

To explore the effect of random variability in nanoparticle distribution within a packing, it is first necessary to generate these random packings. This is done using a discrete element method (DEM) simulation where each particle is defined as a sphere with a corresponding radius and at a position determined by the driving forces between the particles [18]. In this DEM simulation, the nanoparticles are initially placed within a box with random positions and velocity vectors. The nanoparticles are then released and allowed to interact with each other until a stable nanoparticle configuration is achieved. Details of this nanoparticle packing formation process are given in [19].

Fig. 1 illustrates the typical pure copper nanoparticle packings such that four different packings were generated using DEM simulations [19], where the nanoparticles have a mean radius of 116 nm and a standard deviation of 48 nm. This size distribution of particles was chosen because it has been observed from our previous studies [20, 21] that the typical copper nanoparticle ink used in the experimental portion of this study has a log-normal particle size distribution with a 116 nm mean radius and 48 nm standard deviation.
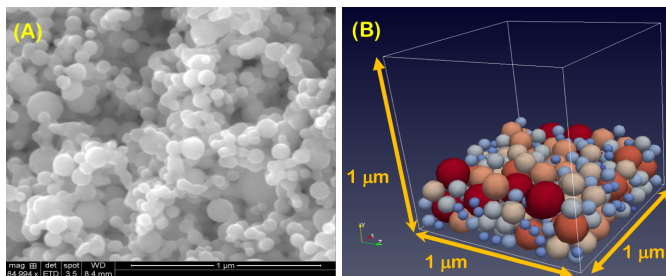

Fig. 1. Copper nanoparticle packings: (A) SEM picture of typical copper nanoparticle packing (B) Copper nanoparticle packing generated by DEM that are lognormally distributed, 116 nm mean radius and 48 nm standard deviation

Once the nanoparticle packings have been built, the effect of nanoparticle packing configuration on their thermo-optical properties can be investigated by applying both TE and TM polarized illumination to the nanoparticle packings and calculating the absorption, scattering, and extinction cross-sections of the nanoparticle packings. In these cross-section calculations, Maxwell's equations are solved by using the Finite Difference Frequency Domain method to obtain the scattered

electric field, and the time-averaged Poynting vector for the time-harmonic field. The absorption cross-section is found by the integration of energy flux over the volume of all particles, and the scattering cross-section is calculated by surface integration of the scattered Poynting vector over an imaginary sphere covering all nanoparticles [14, 21]. These results are then compared to the absorptivity value obtained from spectroscopy measurements of copper nanoparticle packings.

EXPERIMENTAL MEASUREMENT

The absorptivity of the nanoparticle packings by spreading a thin layer of copper nanoparticles (~ 400 nm thick) on a glass substrate was measured experimentally using UV-Vis-NIR spectroscopy, as shown in Fig. 2. For this study, a Cary 5000 UV-Vis-NIR (Agilent Technologies) was used to measure the transmittance, T, and reflectance, R, of the nanoparticle packings over a wavelength range of 400-1064 nm. The absorptivity, A, is then calculated as a function of wavelength from energy conservation using the equation: $A=1-R-T$.
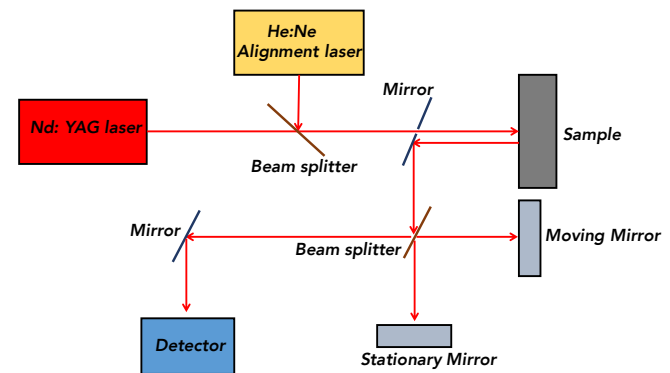
Fig. 2. Schematic of the spectroscopy measurement

RESULTS

Optical absorption of nanoparticle packings has been analyzed both experimentally and via computational simulations for wavelengths between 400 nm and 1064 nm. For both TE and TM polarizations, the simulated absorption cross-section is observed to decrease with increasing wavelength for wavelengths greater than 532 nm. Both the experimentally measured absorptivity and the simulated absorption cross-section reach their maximum values at wavelengths of 532 nm and below, with only small differences between the values at 400 nm and 532 nm. Fig. 3 shows the both measured absorptivity and the simulated absorption cross-section for the four nanoparticle packings generated by DEM, which was also provided in our previous work [20]. These have average absorption cross-sections of ~9.7 x 10^{-13} m^2 for 400 nm and 532 nm, TE and TM polarized light. The absorption cross-section is essentially observed polarization independent, which is as expected due to the isotropic nature of the particle distribution onto the substrate.
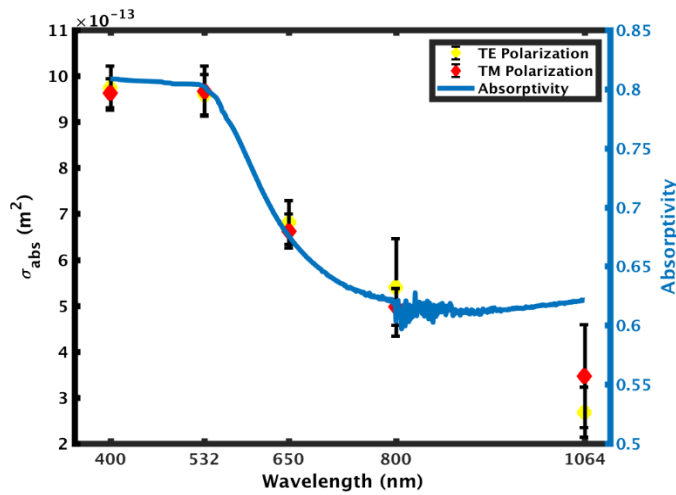
Fig. 3. Simulated absorption cross-section (σ_{abs} (m^2)) and measured absorptivity vs. wavelength (nm) under TE and TM polarized laser illumination.

Overall, the wavelength dependence of the calculated absorption cross-section matches well with that of the experimental absorptivity measurements for the four analyzed nanoparticles packings, as shown in Fig. 3. Relatively flat absorptivity is observed from 400 nm up to 532 nm from both simulations and experimental analysis. Absorption starts to decrease with increasing wavelength from 532 nm up to 800 nm. However, the measured absorptivity levels off at about 0.62 whilst the simulated absorption cross-section continues to decrease with increasing wavelength above 800 nm. A number of possible factors may contribute to this difference.

One potential source is the few-nanometer thick polyvinylpyrrolidone (PVP) coatings applied to the pure copper nanoparticles to prevent the pure copper nanoparticles from agglomeration and oxidization in experimental characterization [20, 21]. The PVP coating is not modeled in the numerical analysis in this work. It is possible that the effect of the PVP coating on thermo-optical behavior could be more important at wavelengths longer than 800 nm. Specifically, surface plasmon dispersion relations and near-field plasmon coupling are affected by particle size and distribution, particle shape, dielectric coating and suspended medium characteristics, and overall nanoparticle packing structure [22, 23, 24]. Electromagnetic energy transfer within arrangements such as disordered nanoparticle chain arrays can be driven by collective plasmon modes [25, 26]. Such collective plasmons within closely spaced nanoparticles result in very high near-field confinement of plasmons within the nano-gaps leading to highly non-localized energy transport between the nanoparticles, and dielectric coating of metal nanoparticles leads to changes in plasmonic behavior and the overall optical response of the nanoparticle packing in the literature [27, 28]. An additional factor may be that near-field coupling between the nanoparticles can be influenced by plasmon hybridization [29, 30, 31] and for many types of particle clusters or packing structures, a second local peak at higher wavelengths is typically observed due to the contribution of higher order plasmon modes (i.e quadrupole modes, etc.) [22, 32]. Thus, the

effective optical property of the PVP coating along with the randomness of the nanoparticle packing which leads to having different nanoparticle chain lengths and structure can result in a higher order resonant frequency shift for the simulated and the measured absorption at wavelengths at near-infrared. This implies that the effect of the coating on higher order plasmon modes within the disordered copper nanoparticle packing could be especially important to predict the resonant wavelength at longer wavelengths. It should also be noted that the actual nanoparticles in the experimental packings are not exact spheres as assumed in the DEM simulation, which could also influence the absorption spectrum. Furthermore, the directionality of the electromagnetic scattering (i.e non-directional or asymmetric scattering) and multipolar resonance effect for different particle sizes spaced closely each other and placed on a glass substrate could also be important at wavelengths longer than 800 nm.
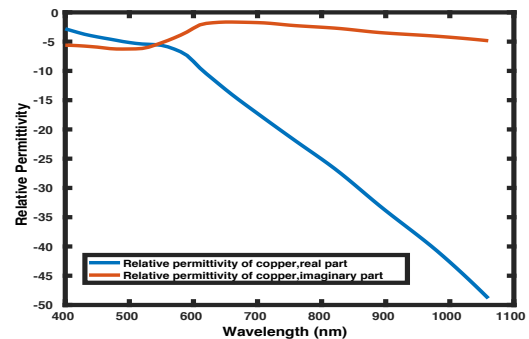
The skin depth might also play an important role in explaining this deviation at higher wavelengths. The skin depth (δ) of a nanoparticle, shown in Fig 4, is calculated as:

$$\delta = \frac{1}{Re\sqrt{-k_0^2 \varepsilon_r}} \qquad (1)$$

where k_0 is the free space wavenumber, and ε_r represents the complex relative permittivity function which is shown in Fig.5 [33].
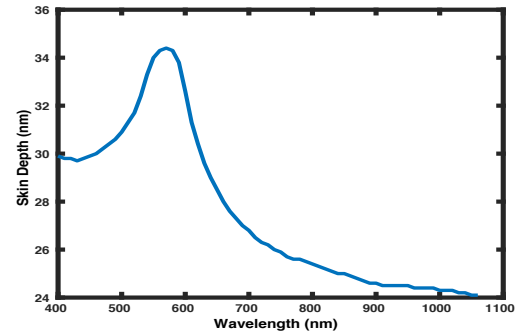
**Fig. 4. Skin Depth vs. wavelength for copper nanoparticle**

Fig. 5. Relative Permittivity vs. wavelength for copper nanoparticle

The skin depth of a copper nanoparticle peaks between 500 nm and 600 nm, then decreases at longer wavelengths, which is also where the numerical and experimental absorption results start to deviate. This decrease in skin depth at longer wavelengths may be significant as it is accompanied by an

increasing difference between the skin depth and electron mean free path in copper. At 532 nm wavelength, the electron mean free path in copper, which is around 36 nm, is almost equal to the skin depth in copper; however, the skin depth is only about two thirds of the mean free path at 1064 nm wavelength. Therefore, the numerical calculation from the finite element method (FEM) simulations could deviate from experiment at higher wavelengths due to the increased importance of quantum effects in the particles which is not taken into consideration in the numerical analysis [34, 35, 36]. The decreased skin depth also results in extra collisions between the electrons and increases the damping within closely spaced nanoparticle packings, which could also reduce the accuracy of the magnetic and electric field calculations. It should also be noted that new theoretical models and experiments are required to characterize the sub-nanometer length-scale quantum effects fully for nanoparticles spaced less than few nanometers in which such effects are not considered in this work [37, 38].

Scattering and Extinction Analysis of Nanoparticle Packings

Scattering cross-section as a function of incoming laser wavelength for both polarizations (TE and TM) is shown in Fig. 6. It is observed that scattering cross-section becomes highest average value ($\sim 7.5 \times 10^{-13}$ m^2) at 532 nm wavelength for both TE and TM polarized laser light. This is due to the surface plasmon polariton generation and near-field scattering at 532 nm wavelength for copper nanoparticles. At 1064 nm, the scattering cross-section reaches its lowest average value of $\sim 5 \times 10^{-13}$ m^2 within the analyzed wavelength range. Moreover, higher average scattering cross-section on TE polarized than TM polarized illumination for each wavelength is observed. However, this result is not statically significant and could be due to the effect of particle distribution and particular particle sizes generated by the DEM in the simulations.
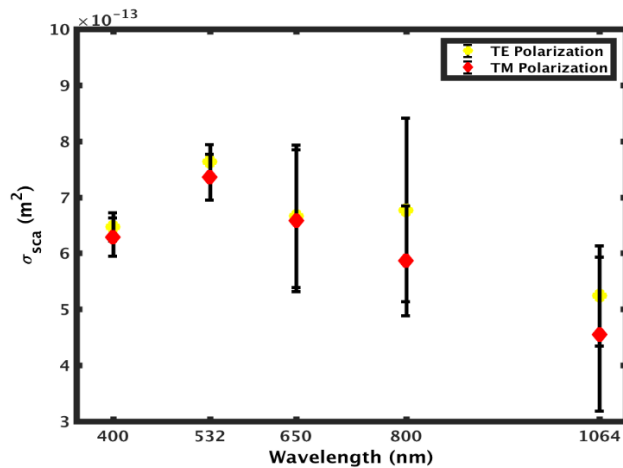
Fig. 6. Calculated scattering cross-sections (σ_{sca} (m^2)) vs. wavelength under TE and TM polarized laser illumination

The far-field radiation pattern, E_{far}, can be obtained by integrating the near-field electric and magnetic fields over an arbitrary surface S_{arb} and in a given direction $\hat{r}$ surrounding the nanoparticles by using the formula given by [39]:

$$E_{far}(\hat{r}) = \frac{ik}{4\pi}\hat{r} \times \int_{S_{arb}} [\hat{n} \times E - \eta\hat{r} \times (\hat{n} \times H)]e^{ik\hat{r}\cdot\hat{r}} dS'$$

where k is the wavenumber, η is the impedance, and $\hat{n}$ is the unit vector normal to the surface S_{arb}.
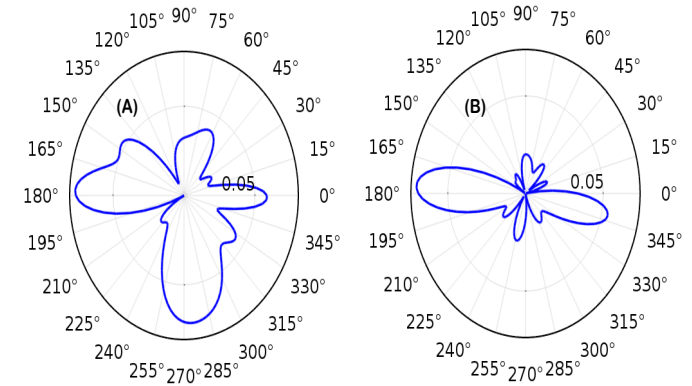
Fig. 7. Far-field radiation pattern of 116 nm mean and 48 nm standard deviation copper nanoparticle packing under 532 nm, TE polarized: (A) xz plane (B) xy plane

Fig. 7 shows the angular distribution of radiation scattered from representative nanoparticle packing under 532 nm and TE polarized light source. All the packings simulated in this study showed similar types of patterns to those presented in Fig. 7 under 532 nm and TE polarized light illumination. It was observed from these far-field radiation patterns that light scattering occurs primarily in the forward direction for the 532 nm, TE polarized light; in other words, the forward scattering through glass substrate is dominant over backward scattering. This forward scattering is in fact characterized by the interferences between magnetic and electric response and the contribution of the plasmon modes, which is affected by the substrate and the particle size distribution. Also, strong sidelobs are observed in the far-field radiation pattern due to the effect of the reflections within the nanoparticle packing on a glass substrate. Overall, spatial distribution of light scattering is observed as asymmetric and directional dependent. This result is somewhat expected because the nanoparticle packing has different particle sizes which are also smaller than the wavelength of the incident laser illumination. It is also interesting that the strength of the sidelobs are also comparable with the strength of the forward scattering. This implies that the magnitude of the unwanted scattering and the transmitted light to the glass substrate is close to each other. Such unwanted scattering is desired to be eliminated to help transport of energy delivered to the layers below the current layer being sintered and improve the bonding between the sintered layers.
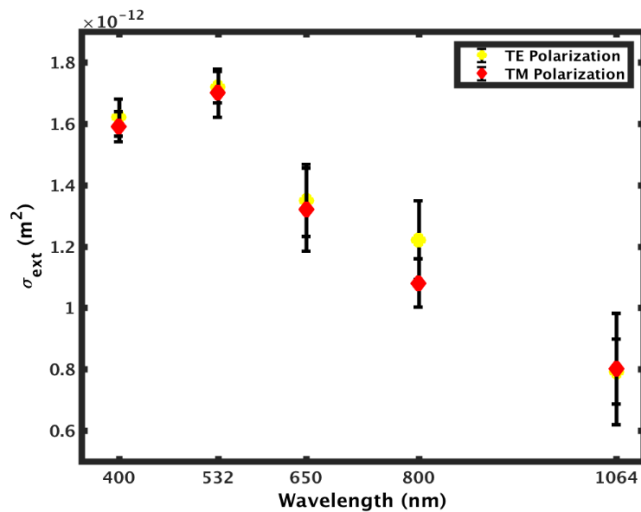
Fig. 8. Calculated extinction cross-sections (σ_{ext} (m²)) vs. wavelength under TE and TM polarized laser illumination

Extinction cross-section as a function of incoming laser wavelength for both polarization (TE and TM) is shown in Fig. 8. It is observed that extinction cross-section becomes a maximum (~1.7 x 10^{-12} m²) at 532 nm wavelength for TE and TM polarized laser wavelength. Extinction cross-section also decreases with increasing wavelengths longer than 532 nm and becomes a minimum (~0.8 x 10^{-12} m²) at 1064 nm illumination. Almost a 50 % reduction in the extinction cross-section is possible by using 1064 nm laser wavelength compared to 532 nm, which implies that light penetration into a nanoparticle packing is affected significantly between 532 nm and 1064 nm wavelength illumination. Also, almost the same average extinction cross-section value is obtained for each TE and TM polarized light which shows the polarization of the light source is not a significant factor on the extinction cross-section between 400-1064 nm wavelengths.
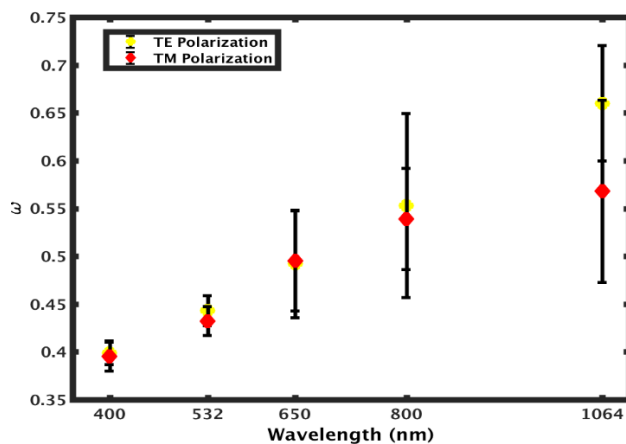
Fig. 9. Simulated single-scatter albedo (ω) vs. wavelength under TE and TM polarized laser illumination

Fig. 9 shows the simulated single-scatter albedo (ω) vs. wavelength under TE and TM polarized laser illumination. It is

observed that ω increases with increasing wavelength from 400 nm to 1064 nm, indicating that the overall extinction is due mainly to scattering at longer wavelengths. At a wavelength of around 650 nm, ω is approximately 0.5 which implies that the scattering and absorption cross-sections are approximately equal. Thus, absorption becomes more important than scattering at wavelengths less than 650 nm but scattering starts to be dominant for copper nanoparticle packings that have a log-normal particle size distribution with a 116 nm mean radius and 48 nm standard deviation, and deposited onto ~400 nm thick glass substrate at wavelengths greater than 650 nm.

CONCLUSION

This study has analyzed optical absorption, scattering, and extinction cross-sections for different copper nanoparticle packings placed on a glass substrate and quantified the influence of variability in nanoparticle distributions on these properties. Collective plasmon modes which are generated within these disordered and closely spaced nanoparticle distributions are potentially affected by the particle size, coating, particle shape, packing structure and substrate. The detailed analysis showed that simulations matched very well with the experimental measurements between 400 nm and 800 nm wavelengths for copper nanoparticle packings that have a log-normal particle size distribution with 116 nm mean radius and 48 nm standard deviation, and deposited onto ~ 400 nm thick glass substrate. It was observed that the uncertainty in the nanoparticle configuration can lead to 15-25 % variation (one sigma) in the thermo-optical properties of the nanoparticle packings at wavelengths between 400 nm and 1064 nm. The highest absorption and extinction cross-section are obtained around 532 nm wavelength illumination and polarization of the light source is not observed a significant effect on thermo-optical properties. At wavelengths above 532 nm, variability in the structure of the nanoparticle packings on the computed scattering starts to increase. It is possible that the effect of few-nanometer thick PVP coating applied onto pure copper nanoparticles on thermo-optical behavior could be more important at wavelengths longer than 800 nm although more analyses are needed to fully understand this phenomenon.

This study demonstrates that illumination wavelength can have a major effect on how energy translates into heat within the nanoparticle packings. Overall, however, polarization and the exact particle locations in the copper nanoparticle packings that have a log-normal particle size distribution with 116 nm mean radius and 48 nm standard deviation, and placed on ~400 nm thick glass substrate are not observed strong effect on absorption between 400 nm and 800 nm wavelength illumination, which means that precise control over the exact location of nanoparticles within the packing should not be necessary to get good uniformity in photonic sintering within photonic nanoparticle sintering processes for the investigated cases between 400 nm and 800 nm wavelength illumination.

would also like to thank N. Roy for the SEM picture presented in Fig. 1 (A) and associated particle size analysis.

REFERENCES

[1] Nayak, L., Mohanty, S., Nayak, S. K., & Ramadoss, A. (2019). A review on inkjet printing of nanoparticle ink for flexible electronics. Journal of Materials Chemistry C.

[2] Mohammed, M. G., & Kramer, R. (2017). All-Printed Flexible and Stretchable Electronics. Advanced Materials, 29(19), 1604965.

[3] Lee, Y., Choi, J. R., Lee, K. J., Stott, N. E., & Kim, D. (2008). Large-scale synthesis of copper nanoparticles by chemically controlled reduction for applications of inkjet-printed electronics. Nanotechnology, 19(41), 415604.

[4] Shemelya, C., Banuelos-Chacon, L., Melendez, A., Kief, C., Espalin, D., Wicker, R., ... & MacDonald, E. (2015, November). Multi-functional 3D printed and embedded sensors for satellite qualification structures. In 2015 IEEE SENSORS (pp. 1-4). IEEE.

[5] Xie, L., Yang, G., Mantysalo, M., Xu, L. L., Jonsson, F., & Zheng, L. R. (2012). Heterogeneous integration of bio-sensing system-on-chip and printed electronics. IEEE Journal on Emerging and Selected Topics in Circuits and Systems, 2(4), 672-682.

[6] Mariotti, C., Su, W., Cook, B. S., Roselli, L., & Tentzeris, M. M. (2014). Development of low cost, wireless, inkjet printed microfluidic RF systems and devices for sensing or tunable electronics. IEEE Sensors Journal, 15(6), 3156-3163.

[7] Xu, L., Karunakaran, R. G., Guo, J., & Yang, S. (2012). Transparent, superhydrophobic surfaces from one-step spin coating of hydrophobic nanoparticles. ACS applied materials & interfaces, 4(2), 1118-1125.

[8] Fuller, S. B., Wilhelm, E. J., & Jacobson, J. M. (2002). Ink-jet printed nanoparticle microelectromechanical systems. Journal of Microelectromechanical systems, 11(1), 54-60.

[9] Rahman, T., Renaud, L., Heo, D., Renn, M., & Panat, R. (2015). Aerosol based direct-write micro-additive fabrication method for sub-mm 3D metal-dielectric structures. Journal of Micromechanics and Microengineering, 25(10), 107002.

[10] Roy, N., Yuksel, A., & Cullinan, M. (2016). Design and modeling of a microscale selective laser sintering system. In *ASME 2016 11th International Manufacturing Science and Engineering Conference*. American Society of Mechanical Engineers Digital Collection.

[11] Yuksel, A., Edward, T. Y., Cullinan, M., & Murthy, J. (2019). Effect of particle size distribution on near-field thermal energy transfer within the nanoparticle packings. Journal of Photonics for Energy, 9(3), 032707.

[12] Yuksel, A., Yu, E. T., Cullinan, M., & Murthy, J. (2018). Heat Transfer Modeling of Nanoparticle Packings on a Substrate. In *ASME 2018 International Mechanical Engineering Congress and Exposition*. American Society of Mechanical Engineers Digital Collection.

[13] Yuksel, A., Cullinan, M., & Murthy, J. (2017). Thermal energy transport below the diffraction limit in close-packed metal nanoparticles. In *ASME 2017 Heat Transfer Summer Conference*. American Society of Mechanical Engineers Digital Collection.

[14] Yuksel, A., Edward, T. Y., Murthy, J., & Cullinan, M. (2017). Effect of Substrate and Nanoparticle Spacing on Plasmonic Enhancement in Three-Dimensional Nanoparticle Structures. Journal of Micro and Nano-Manufacturing, 5(4), 040903.

[15] Yuksel, A., Cullinan, M., & Murthy, J. (2017). Polarization effect on out of plane configured nanoparticle packing. In *ASME 2017 12th International Manufacturing Science and Engineering Conference collocated with the JSME/ASME 2017 6th International Conference on Materials and Processing*. American Society of Mechanical Engineers Digital Collection.

[16] Yuksel, A., Edward, T. Y., Cullinan, M., & Murthy, J. (2017). Analysis of near-field thermal energy transfer within the nanoparticles. In Plasmonics: Design, Materials, Fabrication, Characterization, and Applications XV (Vol. 10346, p. 103462X). International Society for Optics and Photonics.

[17] Roper, D. K., Ahn, W., & Hoepfner, M. (2007). Microscale heat transfer transduced by surface plasmon resonant gold nanoparticles. The Journal of Physical Chemistry C, 111(9), 3636-3641.

[18] Kruggel-Emden, H., Simsek, E., Rickelt, S., Wirtz, S., & Scherer, V. (2007). Review and extension of normal force models for the discrete element method. Powder Technology, 171(3), 157-173.

[19] Yuksel, A., & Cullinan, M. (2016). Modeling of nanoparticle agglomeration and powder bed formation in microscale selective laser sintering systems. Additive Manufacturing, 12, 204-215.

[20] Yuksel, A., Edward, T. Y., Cullinan, M., & Murthy, J. (2018). Uncertainty Analysis of Near-Field Thermal Energy Transfer within Nanoparticle Packing. In *2018 17th IEEE Intersociety Conference on Thermal and Thermomechanical Phenomena in Electronic Systems (ITherm)* (pp. 46-50). IEEE.

[21] Yuksel, A., Yu, E. T., Cullinan, M., & Murthy, J. (2020). Thermal Transport in Nanoparticle Packings Under Laser Irradiation. *Journal of Heat Transfer*, 142(3).

[22] Taylor, R. W., Esteban, R., Mahajan, S., Aizpurua, J., & Baumberg, J. J. (2016). Optimizing SERS from gold

nanoparticle clusters: addressing the near field by an embedded chain plasmon model. *The Journal of Physical Chemistry C*, *120*(19), 10512-10522.

[23] Miller, M. M., & Lazarides, A. A. (2005). Sensitivity of metal nanoparticle surface plasmon resonance to the dielectric environment. *The Journal of Physical Chemistry B*, *109*(46), 21556-21565.

[24] Lim, D. K., Barhoumi, A., Wylie, R. G., Reznor, G., Langer, R. S., & Kohane, D. S. (2013). Enhanced photothermal effect of plasmonic nanoparticles coated with reduced graphene oxide. *Nano letters*, *13*(9), 4075-4079.

[25] Maier, S. A., Kik, P. G., & Atwater, H. A. (2002). Observation of coupled plasmon-polariton modes in Au nanoparticle chain waveguides of different lengths: Estimation of waveguide loss. *Applied Physics Letters*, *81*(9), 1714-1716.

[26] Kravets, V. G., Schedin, F., Kabashin, A. V., & Grigorenko, A. N. (2010). Sensitivity of collective plasmon modes of gold nanoresonators to local environment. *Optics letters*, *35*(7), 956-958.

[27] Chanana, M., & Liz-Marzan, L. M. (2012). Coating matters: the influence of coating materials on the optical properties of gold nanoparticles. *Nanophotonics*, *1*(3-4), 199-220.

[28] Yang, Z. J., Wang, Q. Q., & Lin, H. Q. (2013). Tunable two types of Fano resonances in metal–dielectric core–shell nanoparticle clusters. *Applied Physics Letters*, *103*(11), 111115.

[29] Prodan, E., & Nordlander, P. J. C. P. (2004). Plasmon hybridization in spherical nanoparticles. *The Journal of chemical physics*, *120*(11), 5444-5454.

[30] Prodan, E., Radloff, C., Halas, N. J., & Nordlander, P. (2003). A hybridization model for the plasmon response of complex nanostructures. *science*, *302*(5644), 419-422.

[31] Thiessen, E., Heinisch, R. L., Bronold, F. X., & Fehske, H. (2016). Surface mode hybridization in the optical response of core-shell particles. *Physical Review A*, *93*(3), 033827.

[32] Wang, H. (2018). Plasmonic refractive index sensing using strongly coupled metal nanoantennas: nonlocal limitations. *Scientific reports*, *8*(1), 1-8.

[33] Johnson, P. B., & Christy, R. W. (1972). Optical constants of the noble metals. Physical review B, 6(12), 4370.

[34] Tan, S. F., Wu, L., Yang, J. K., Bai, P., Bosman, M., & Nijhuis, C. A. (2014). Quantum plasmon resonances controlled by molecular tunnel junctions. Science, 343(6178), 1496-1499.

[35] Betzig, E., & Trautman, J. K. (1992). Near-field optics: microscopy, spectroscopy, and surface modification beyond the diffraction limit. Science, 257(5067), 189-195

[36] Boto, A. N., Kok, P., Abrams, D. S., Braunstein, S. L., Williams, C. P., & Dowling, J. P. (2000). Quantum interferometric optical lithography: exploiting entanglement to beat the diffraction limit. Physical Review Letters, 85(13), 2733.

[37] Esteban, R., Borisov, A. G., Nordlander, P., & Aizpurua, J. (2012). Bridging quantum and classical plasmonics with a quantum-corrected model. *Nature communications*, *3*(1), 1-9.

[38] Savage, K. J., Hawkeye, M. M., Esteban, R., Borisov, A. G., Aizpurua, J., & Baumberg, J. J. (2012). Revealing the quantum regime in tunnelling plasmonics. *Nature*, *491*(7425), 574-577.

[39] Stratton, J. A., & Chu, L. J. (1939). Diffraction theory of electromagnetic waves. Physical Review, 56(1), 99.